Assessment of the pseudo-tracking approach for the calculation of material acceleration and pressure fields from time-resolved PIV

Part I. Error propagation

Van Gent, P. L.; Schrijer, F. F.J.; Van Oudheusden, B. W.

DOI
10.1088/1361-6501/aaa0a5

Publication date
2018

Document Version
Final published version

Published in
Measurement Science and Technology

Measurement Science and Technology

PAPER

Assessment of the pseudo-tracking approach for the calculation of material acceleration and pressure fields from time-resolved PIV: part I. Error propagation

To cite this article: P L van Gent *et al* 2018 *Meas. Sci. Technol.* **29** 045204

IOP Publishing Measurement Science and Technology
Meas. Sci. Technol. **29** (2018) 045204 (14pp) https://doi.org/10.1088/1361-6501/aaa0a5

Assessment of the pseudo-tracking approach for the calculation of material acceleration and pressure fields from time-resolved PIV: part I. Error propagation

P L van Gent, F F J Schrijer and B W van Oudheusden

Faculty of Aerospace Engineering, Delft University of Technology, Netherlands

E-mail: p.l.vangent@tudelft.nl

Received 10 October 2017, revised 30 November 2017
Accepted for publication 5 December 2017
Published 7 March 2018

Abstract

Pseudo-tracking refers to the construction of imaginary particle paths from PIV velocity fields and the subsequent estimation of the particle (material) acceleration. In view of the variety of existing and possible alternative ways to perform the pseudo-tracking method, it is not straightforward to select a suitable combination of numerical procedures for its implementation. To address this situation, this paper extends the theoretical framework for the approach. The developed theory is verified by applying various implementations of pseudo-tracking to a simulated PIV experiment. The findings of the investigations allow us to formulate the following insights and practical recommendations: (1) the velocity errors along the imaginary particle track are primarily a function of velocity measurement errors and spatial velocity gradients; (2) the particle path may best be calculated with second-order accurate numerical procedures while ensuring that the CFL condition is met; (3) least-square fitting of a first-order polynomial is a suitable method to estimate the material acceleration from the track; and (4) a suitable track length may be selected on the basis of the variation in material acceleration with track length.

Keywords: PIV, pseudo-tracking, pressure, material acceleration

(Some figures may appear in colour only in the online journal)

1. Introduction

The material derivative of flow velocity, also referred to as the material acceleration, represents the flow acceleration from a Lagrangian perspective. It is related to the spatial pressure gradient according to the momentum equation and can therefore be used to determine instantaneous pressure fields (van Oudheusden 2013). The availability of such pressure fields allows the analysis of flow dynamics beyond those based on velocity fields and surface pressure data, which are more commonly available from experiments (Ghaemi and Scarano 2013, Liu and Katz 2013, Pröbsting *et al* 2013, Joshi *et al* 2014) and may alleviate the need for surface pressure measurements. In view of these prospects, the experimental determination of the material acceleration has been subject of extensive research and different methods have been proposed.

Using digital image recordings of flows which have been seeded with tracer particles, the material acceleration can be extracted from velocity fields obtained through correlation analysis, i.e. particle image velocimetry (PIV), or more directly by tracking particle patterns (e.g. Lynch and Scarano (2013) and Jeon *et al* (2014)) or individual particles (e.g. Schanz *et al* (2016)). Recently, van Gent *et al* (2017a) reported a study that compared a variety of these different approaches using a simulated experiment, which was carried out in the context of NIOPLEX, an FP7 project centred around pressure determination from particle-based data. The comparison showed that techniques based on novel direct particle tracking

approaches (Shake-The-Box, Schanz *et al* (2016)), in combination with advanced algorithms (FlowFit, Gesemann *et al* (2016) or VIC+, Schneiders and Scarano (2016)) could produce more accurate pressure reconstructions than PIV-based approaches due to a higher spatial resolution and better use of time information in the data sets.

In view of their novelty, determining the extent to which the observed benefits of direct particle tracking approaches apply to actual physical experiments arguably requires additional experimental assessments. The performance of PIV in terms of velocity measurement has on the other hand been characterised and demonstrated in a large number of experiments covering a wide range of applications (Raffel *et al* 2007, Scarano 2013). Either way, PIV may be the most suitable, if not the only feasible approach when it is not possible to reliably (directly) track a dense collection of particles over a reasonable distance and duration, e.g. because of insufficient image quality, insufficient control of seeding density, insufficient temporal resolution, or in the case of thin or planar measurement domain, where particles quickly leave the domain due to out-of-plane motions (as noted by Wang *et al* (2017)).

Using at least two PIV velocity fields closely separated in time, the material acceleration can be calculated using a Eulerian (e.g. Baur and Köngeter (1999)) or Lagrangian formulation (e.g. Jensen *et al* (2003) and Liu and Katz (2006)). In the Eulerian approach, local temporal and spatial velocity derivatives are first determined separately (Christensen and Adrian 2002, Foucaut and Stanislas 2002, Perret *et al* 2006) and then combined to compose the material acceleration. In the Lagrangian approach, the measured PIV velocity fields are seeded with imaginary particles that are traced forward and backward in time. The material acceleration is then obtained from the variation in velocity values at subsequent imaginary particle positions. Approaches based on this principle are also referred to as pseudo-tracing or -tracking, for the reason that the particle trajectories are not available from the measurement directly, but are constructed afterwards.

de Kat and van Oudheusden (2012) showed that for successful implementation of the Eulerian and pseudo-tracking methods, the time separation between subsequent velocity fields needs to be at least 10 times smaller than the Eulerian and Lagrangian time scales of the flow, respectively. Furthermore, several studies found that for advection-dominated flow phenomena the pseudo-tracking is less sensitive to noise (Jensen and Pedersen 2004, Violato *et al* 2011, de Kat and van Oudheusden 2012, Ghaemi *et al* 2012, van Oudheusden 2013, van Gent *et al* 2017a). Which methods yields the most accurate results therefore depends on the nature of the flow, the achievable acquisition frequency, and the level of measurement noise. The present study focusses on the pseudo-tracking method.

Originally, pseudo-tracking was applied using only two velocity fields, limiting the temporal length and resolution of the imaginary particle track to their respective time separation (Jensen *et al* 2003, Liu and Katz 2006, de Kat and van Oudheusden 2012, Dabiri *et al* 2014). With the development of time-resolved and tomographic PIV, the technique has become increasingly feasible and attractive. The availability of volumetric velocity data allows the calculation of imaginary particle tracks in all spatial dimensions. Furthermore, the availability of time-resolved data allows more accurately calculating longer tracks, limited in length only by the time it takes for the imaginary particle to leave the measurement domain. Using time-resolved, volumetric velocity data, several users of the pseudo-tracking approach therefore calculated tracks over multiple velocity fields (Violato *et al* 2011, Moore *et al* 2011, Ghaemi *et al* 2012, Pröbsting *et al* 2013, Jeon *et al* 2015, Wang *et al* 2017).

Whereas various studies made use of the same basic principles of pseudo-tracking, they differed with respect to its implementation. Using two velocity fields, Jensen *et al* (2003) started the imaginary particle tracks at the first of the two velocity snapshots and obtained the particle position at the time of the second velocity field by implicit second-order trapezoidal integration. The material acceleration was then obtained by central differencing of the velocity values at the two particle positions. A similar approach was followed by Liu and Katz (2006) and Dabiri *et al* (2014). de Kat and van Oudheusden (2012) used a centred approach by starting the track at the time instance between both velocity fields. Furthermore, their study proposed an iterative procedure in which the calculated material acceleration is used to improve the particle track in a next iteration. Moore *et al* (2011) performed multiple integration steps per PIV time step to reduce the truncation error. Pröbsting *et al* (2013) did not estimate the material acceleration from the track by central differencing, but by (ordinary) least-square fitting of a first-order polynomial. This strategy was also adopted by Jeon *et al* (2016), who incorporated it as part of an iterative approach in which both velocity and the material acceleration fields are updated. Wang *et al* (2017) fitted higher-order polynomials in yet another iterative procedure in which only the velocity field is updated.

Given the variety of possible implementations of pseudo-tracking, it is not straightforward to select an optimum combination of numerical methods and the parameters involved. This paper addresses this issue by providing practical guidelines for the use of pseudo-tracking, in particular on how to best construct the imaginary track (integration time step, order of integration and interpolation procedures, and track length) and on how to best estimate the material acceleration from the track. To arrive at these results, the theoretical framework for the approach with respect to error propagation is expanded to include all error sources and their propagation for time-resolved measurements. A numerical assessment is performed to validate the developed theory and to compare the results from different implementations of pseudo-tracking. Since the calculation of material acceleration is often used as an intermediate step in the calculation of pressure fields, this study gives specific attention to pressure results.

The study is part of a wider assessment of the pseudo-tracking method: the present article (part I) focusses on error propagation. A companion article (part II, van Gent *et al* (2017b)) investigates the spatio-temporal filtering behaviour of the method.

The structure of the present article is as follows: section 2 gives an overview of existing implementations of the pseudo-tracking approach and provides a mathematical framework that is used throughout the study. Sections 3 and 4 contain a theoretical and a numerical assessment, respectively. Section 5 proposes a technique to inform the selection of a suitable (pseudo-)track length from experimental data. Finally, section 6 contains a summary of the gained insights as well as practical guidelines for the implementation of pseudo-tracking.

2. Operating principle and implementation

According to the pseudo-tracking approach, the flow field is first 'seeded' with imaginary particles, after which their tracks are calculated through a series of subsequent PIV velocity fields (section 2.1). Material accelerations are then obtained from the variation in particle velocity along the tracks (section 2.2).

2.1. Calculation of imaginary particle tracks

Initially, at time t_0, the imaginary particles are located at the grid points of the PIV velocity fields. Particle tracks are calculated forward and backward in time by numerical integration of the particle velocity, obtained from the PIV velocity data through spatial and temporal interpolation. Different combinations of integration and interpolation methods may be employed.

After $\pm$i integration steps ($\pm$ indicates integration in both time directions), the time is $t_{\pm \mathrm{i}} = t_0 \pm \mathrm{i}\Delta t_{\mathrm{int}}$, where Δt_{int} is the integration time step. At that time, the imaginary particles are located at $\mathbf{x_p}(\pm\mathrm{i}) = \mathbf{x_p}(t_{\pm\mathrm{i}})$ and have a velocity $\mathbf{u_p}(\pm\mathrm{i}) = \mathbf{u}(t_{\pm\mathrm{i}}, \mathbf{x_p}(t_{\pm\mathrm{i}}))$. The total time interval covered by the track is $2\Delta T = 2n_{\mathrm{int}}\Delta t_{\mathrm{int}} = 2n_{\mathrm{piv}}\Delta t_{\mathrm{piv}} = (N_{\mathrm{piv}} - 1)\Delta t_{\mathrm{piv}}$. Here, ΔT is the temporal track length in a single integration direction, n_{int} is the number of integration steps in a single direction, n_{piv} is the number of velocity fields in a single direction and N_{piv} is the total number PIV velocity fields covered by the track. Δt_{piv} is the time separation between the individual velocity fields, which is not necessarily similar to the integration time step Δt_{int}.

2.2. Calculation of material acceleration from the imaginary tracks

In a second step, the material acceleration ($D\mathbf{u}/Dt$) is determined by estimating the first derivative of the velocity at the initial particle position. Two approaches are commonly considered in literature: central differencing (e.g. Liu and Katz (2006) and de Kat and van Oudheusden (2012)),

$$\frac{D\mathbf{u}}{Dt} = \frac{\mathbf{u_p}(n_{\mathrm{int}}) - \mathbf{u_p}(-n_{\mathrm{int}})}{2\Delta T}, \tag{1}$$

and polynomial regression (Pröbsting *et al* 2013, Jeon *et al* 2015, Wang *et al* 2017). The latter approach uses a regression model for each track:

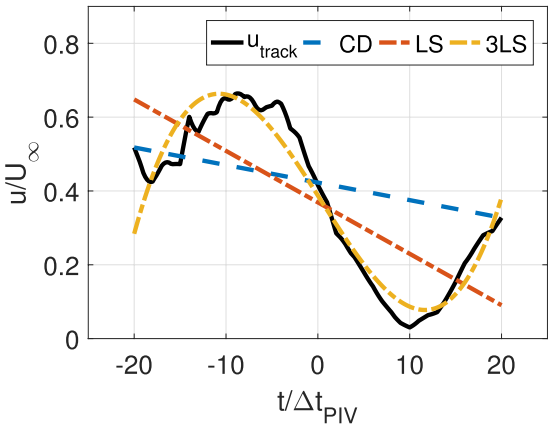

Figure 1. Illustration of three methods to obtain the material acceleration from the constructed track, central differencing (CD), least-square fitting of a first-order (LS) and (3LS) polynomial.

$$\begin{bmatrix} u_p(-n) \\ . \\ u_p(0) \\ . \\ u_p(n) \end{bmatrix} = \begin{bmatrix} 1 & t_{-n} & . & t_{-n}^m \\ . & . & . & . \\ 1 & t_0 & . & t_0^m \\ . & . & . & . \\ 1 & t_n & . & t_n^m \end{bmatrix} \begin{bmatrix} \mathrm{a}_0 \\ \mathrm{a}_1 \\ . \\ \mathrm{a}_m \end{bmatrix} + \begin{bmatrix} \varepsilon_{-n} \\ . \\ \varepsilon_0 \\ . \\ \varepsilon_n \end{bmatrix} \tag{2}$$

or in matrix notation: $\mathbf{u_p} = \mathbf{Ta} + \varepsilon$. For brevity we used $n = n_{\mathrm{int}}$. Alternatively, the model can be defined to only include time instances that coincide with those of PIV velocity fields. $\mathbf{a}$ is a matrix with the coefficients of a polynomial of order m. $\mathbf{Ta}$ is a vector with the (velocity) values according to the polynomial fit and ε is a vector that describes the (unobserved, random) difference between the polynomial and the original velocity along the calculated track.

Equation (2) can be solved in a (ordinary) least-square sense by $\hat{\mathbf{a}} = (\mathbf{T}^T\mathbf{T})^{-1}\mathbf{T}^T\mathbf{u_p}$, where $\hat{\mathbf{a}}$ is the ordinary least-square estimator for $\mathbf{a}$, and $\mathbf{T}^T$ is the transpose of $\mathbf{T}$.

The material acceleration can be identified as the first derivative of the fitted polynomial, i.e. $Du/Dt = \sum_{j=1}^{m} j\mathrm{a}_j\Delta t^{j-1}$. In practice, different tracks in a measurement volume have different lengths due to truncation of the track at the boundaries of the domain. To efficiently implement polynomial fitting, the present implementation takes a *weighted* least-square approach that uses a single fixed nominal track length and assigns a zero weight to any track positions outside the measurement domain via a weighting matrix $\mathbf{W}$, so that $\hat{\mathbf{a}} = (\mathbf{T}^T\mathbf{WT})^{-1}\mathbf{T}^T\mathbf{Wu_p}$.

Figure 1 illustrates the results of central differencing (CD), least-square fitting of a first-order polynomial (LS) and least-square fitting of a third-order polynomial (3LS) through the track velocity. The results in the figure have been obtained for a temporal track length of $40\Delta t_{\mathrm{piv}}$, corresponding to $n_{\mathrm{piv}} = 20$ or equivalently $N_{\mathrm{piv}} = 41$. The material acceleration can be identified from the figure as the slope at $t = 0$. Least-square fitting of a second-order polynomial is not considered as due to the symmetry of the approach in time, it yields identical acceleration results as LS. This can be verified by noting from the Savinsky–Golay tables (e.g. Gorry (1990)) that both approaches have identical convolution coefficients for the determination of the first derivative.

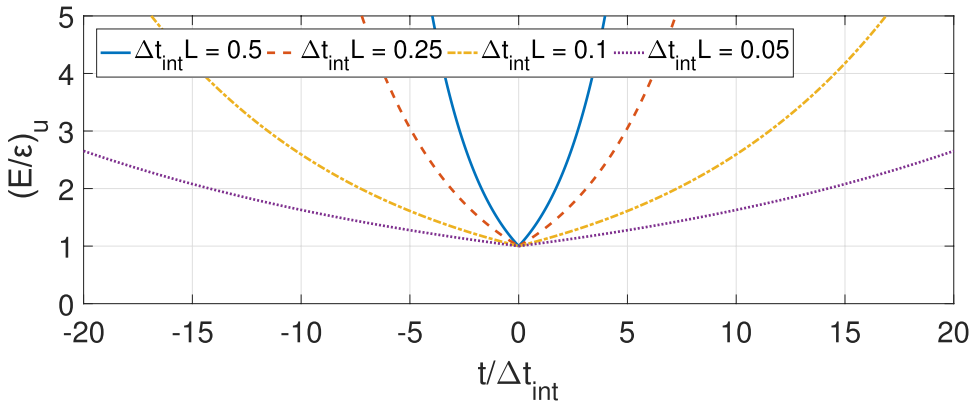

Figure 2. Velocity error bound for different Lipschitz constants.

In addition to the methods shown in figure 1, this study considers an iterative approach (ILS, iterative least-square fitting) in which the track velocity resulting from LS is used to recalculate the track in a next iteration (as inspired by de Kat and van Oudheusden (2012), Jeon *et al* (2016) and Wang *et al* (2017)).

Note that the collection of approaches that can be used to obtain the material acceleration from an imaginary track is not restricted to numerical differentiation and least-square fitting. In fact, a wide range of alternative regression techniques exist that can be used for computing derivatives from noisy data, i.e. the track velocity (e.g. Ahnert and Abel (2007) and Knowles and Renka (2012)). Smoothing splines are for instance used in the context of direct tracking (Gesemann *et al* 2016) i.e. tracking of actual particles seeded in the flow.

3. Theoretical error assessment

Errors are introduced at different points in the procedure outline in section 2. During the construction of the imaginary track, position errors are incurred due to numerical integration and interpolation procedures, due to the propagation of velocity measurement errors, and due to the propagation of position errors from any previous integration steps. The velocity errors along the track are a combination of velocity measurement errors, interpolation errors and propagated position errors, i.e. in presence of spatial velocity gradients, any position error of the imaginary particle leads to an additional velocity error. All errors propagate when estimating the material acceleration from the track velocity, while an additional truncation error is incurred that depends on the numerical procedure used.

3.1. Earlier assessments

Pseudo-tracking has been subject to various error assessments (Jensen and Pedersen 2004, Violato *et al* 2011, de Kat and van Oudheusden 2012, van Oudheusden 2013, Laskari *et al* 2016, McClure and Yarusevych 2017). van Oudheusden (2013) provides an overview of different error analyses, in particular those by Jensen and Pedersen (2004) and de Kat and van Oudheusden (2012). Summarizing the results of these analyses, the standard error in the material acceleration ($\varepsilon^2_{Du/Dt,CD}$) as estimated by central differencing (CD) can be expressed as:

$$\varepsilon^2_{Du/Dt,CD} = \sigma_u^2\left(\frac{1}{2\Delta T^2} + \frac{1}{2}|\nabla \mathbf{u}|^2\right) + \left(\frac{\Delta T^2}{6}\frac{D^3\mathbf{u}}{Dt^3}\right)^2. \quad (3)$$

Here σ_u^2 denotes the variance of the velocity error, while ΔT is the time step used, as defined previously. The first term on the right-hand side represents the propagation of velocity errors, being composed of the direct propagation of the local velocity error ($1/(2\Delta T^2)$) and the propagation of the position error ($\frac{1}{2}|\nabla \mathbf{u}|^2$). The second term on the right-hand side represents the truncation error incurred by the central differencing. The expression shows that the impact of velocity errors reduces with larger time separations (longer tracks), whereas the truncation error increases.

3.2. Extension to longer tracks in time-resolved data

Earlier assessments (section 3.1) did not take into account that when performing multiple integration steps, the position errors incurred at previous integration steps leads to additional position and velocity errors in subsequent integration steps. Furthermore, equation (3) assumes that the local velocity errors at different positions along the particle track are independent from each other. In reality however, the velocity errors along the track can have significant serial correlation, as will be demonstrated in section 4.2 on the basis of a numerical test case. In view of these limitations, the theoretical framework with respect to error propagation is expanded.

With regards to the propagation of position errors from previous integration steps, the derivation in appendix A shows that the global velocity error after n_{int} integration steps ($E_{u,n}$) is bounded to $E_{u,n} \leqslant \varepsilon_{u,\max}(1+\Delta t_{\text{int}}L)^{n_{\text{int}}} \leqslant \varepsilon_{u,\max}\mathrm{e}^{\Delta TL}$ (see appendix; we ignore the truncation error in equation (A.6)). Here $\varepsilon_{u,\max}$ denotes the maximum local velocity error along the track, L is the Lipschitz constant such that $||\mathbf{u}(\mathbf{x_1},t_1) - \mathbf{u}(\mathbf{x_2},t_2)||L \leqslant ||\mathbf{x_1} - \mathbf{x_2}||$. This result shows that the maximum error is strongly dependent on local velocity gradients and may grow exponentially with the time separation $\Delta T = n_{\text{int}}\Delta t_{\text{int}}$. To illustrate this, figure 2 shows the

velocity error bound $E_{u,n} \leqslant \varepsilon_{u,\max}(1+\Delta t_{\text{int}}L)^{n_{\text{int}}}$ for different values of $\Delta t_{\text{int}}L$ as a function of n_{int}.

Whereas the Lipschitz constant allows to define an upper bound, it is assumed here that in a statistical sense, the global velocity error develops according to $E_{u,n} \approx \sigma_u e^{c_{|\nabla u|} n_{\text{piv}}}$, where $c_{|\nabla u|}$ is a position error propagation constant that varies for different tracks. This model assumes that statistically, the errors from spatial and temporal interpolation are small compared to PIV measurement error (σ_u). The validity of the model is demonstrated in section 3.1, which finds that $c_{|\nabla u|} \approx 0.04$ for tracks in separated flow regions with relatively high velocity gradients.

As already mentioned, earlier error assessments (see section 3.1, equation (3)) assumed that the velocity errors at different positions along the particle track are independent from each other, whereas in reality they are not. In fact, the numerical test case in section 4.2 shows average correlation coefficients of up to 0.4 for $n_{\text{piv}} = 3$, depending on the flow region. The presence of such an appreciable correlation is attributed to three causes:

(i) Position errors in the track reconstruction may wrongly guide particles into flow regions with higher or lower velocities than the particles would encounter if they would follow the correct tracks without position errors.
(ii) PIV processing leads to a spatial filtering (see, e.g. Schrijer and Scarano (2008)). The unresolved flow features are typically small so that they convect with the flow. Any errors associated with the spatial filtering therefore also convect.
(iii) The PIV measurement may lead to systematic errors (e.g. particle slip and calibration errors) in certain flow regions. Errors along particle tracks in these regions are therefore correlated in time.

The correlation of velocity errors along a track has two important consequences. Firstly, in the track construction, it leads to increased error accumulation as the position error incurred during a integration step is less likely to (partly) compensate for the position error made in a previous step. Note that the derived bound $E_{u,n} \leqslant \varepsilon_{u,\max} e^{\Delta TL}$ does not take into account that some errors may cancel each other. Secondly, during the estimation of the material acceleration from the imaginary track, the correlation leads to a less effective reduction of the impact of noise with longer track lengths. This latter effect is investigated further below.

Using the model for error propagation derived above $E_{u,n} \approx \sigma_u e^{c_{|\nabla u|} n_{\text{piv}}}$, and accounting for serial correlation, the standard error in material acceleration obtained by central differencing can now be expressed as

$$\varepsilon^2_{Du/Dt,CD} = \sigma_u^2 \left(\frac{e^{2c_{|\nabla u|} n_{\text{piv}}}(1-\rho_{2\Delta T})}{2\Delta T^2} \right) + \left(\frac{\Delta T^2}{6} \frac{D^3\mathbf{u}}{Dt^3} \right)^2 + \varepsilon^2_{\lambda<2WS}$$
$$= \varepsilon^2_{n,CD} \frac{\sigma_u^2}{\Delta t^2_{\text{piv}}} + \left(\frac{\Delta T^2}{6} \frac{D^3\mathbf{u}}{Dt^3} \right)^2 + \varepsilon^2_{\lambda<2WS} \quad (4)$$

$$\text{where,} \quad \varepsilon^2_{n,CD} = \frac{e^{2c_{|\nabla u|} n_{\text{piv}}}(1-\rho_{2\Delta T})}{2n^2_{\text{piv}}}.$$

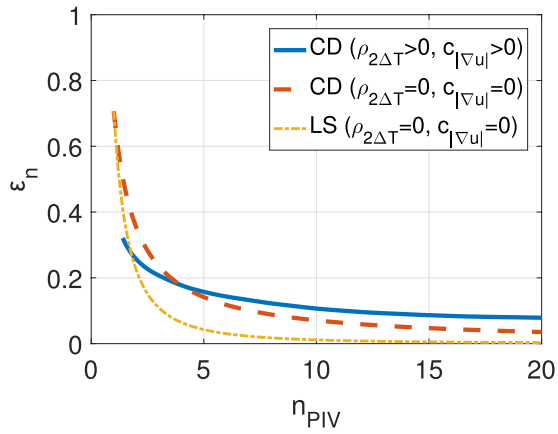

Figure 3. Noise amplification for centred differencing (CD) and least-square fitting (LS).

Here $\rho_{2\Delta T}$ denotes the correlation coefficient indicating the correlation of the velocity errors at the track extremes. Since central differencing considers the difference in velocities at the track extremes, a higher correlation value (which corresponds to a smaller difference in velocity error levels) leads to a lower acceleration error. $\varepsilon_{n,CD}$ is a velocity error amplification coefficient analogous to Foucaut and Stanislas (2002). As mentioned, $\Delta T = n_{\text{int}}\Delta t_{\text{int}} = n_{\text{piv}}\Delta t_{\text{piv}}$ represents the time covered by the track in a single direction (so forward or backward). $\varepsilon^2_{\lambda<2WS}$ is the variance of the error due to spatial filtering by the PIV measurement. As a result of this filtering, any flow scale smaller than about two window sizes is highly modulated and can therefore not be properly reproduced by pseudo-tracking.

Temporal filtering of PIV is disregarded here as the time separation in time-resolved PIV measurements is typically smaller than the relevant time scales of the flow. In case of pseudo-tracking between only two velocity fields separated by $\Delta T > \Delta t_{\text{piv}}$, the error from temporal resolution ($\varepsilon^2_{\lambda<2\Delta T}$) may become significant, however. In addition, the variance of measurement errors (σ_u^2) would need to be replaced by a quantity that includes errors from temporal interpolation, which can no longer be assumed to be small.

Due to the complex dependency of the resulting error in material acceleration on the track length, it is difficult to find an analytical expression for an optimal track length as suggested in Jensen and Pedersen (2004) and McClure and Yarusevych (2017). However, in absence of correlation, $\rho_{2\Delta T} = 0$, it can be shown that the first term on the right-hand side of equation (4) attains a minimum at $\Delta T/\Delta t_{\text{piv}} = n_{\text{piv}} = c^{-1}_{|\nabla u|}$.

Figure 3 shows the velocity error amplification coefficient $\varepsilon_{n,CD}$ according to equation (4) using a position error propagation constant of $c_{|\nabla u|} = 0.04$ and a correlation function $\rho_{2\Delta T}$ as determined from the numerical test case in section 4.2 for flow regions with a large velocity gradient and unresolved flow structures. In addition, the figure shows the velocity error amplification in case of uncorrelated errors ($\rho_{2\Delta T} = 0$) with a constant variance ($c_{|\nabla u|} = 0$) for central differencing (CD) as well as for least-square fitting (LS), see equation (5), section 3.3. The result for $\rho_{2\Delta T} > 0$ and $c_{|\nabla u|} > 0$ corresponds to flow regions with a large velocity gradient and unresolved

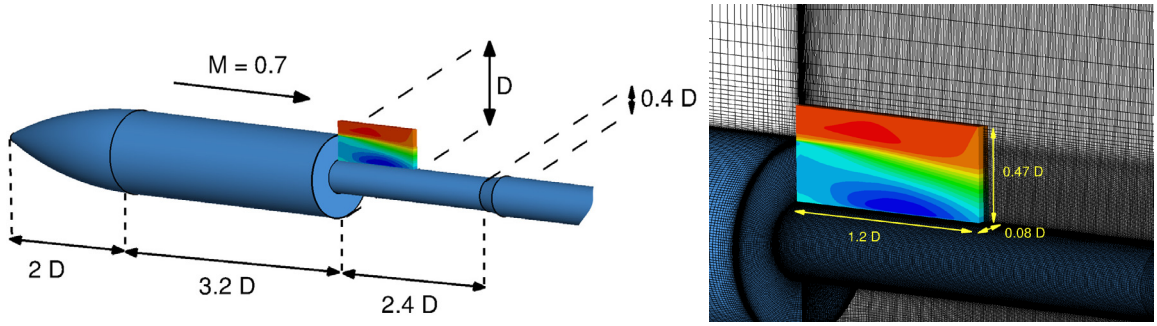

(a) (b)

Figure 4. Test geometry: (a) overview and (b) detail of the numerical mesh in the base-flow region (D is the main body diameter); the coloured insert indicates the extracted region to define the simulated experiment; filled colour contours depict the mean streamwise velocity (Reproduced with permission from van Gent *et al* (2017a) © The Author(s) 2017. This article is an open access publication. With permission of Springer).

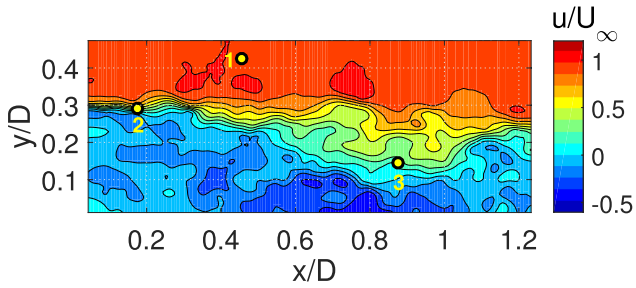

Figure 5. Representative example of instantaneous streamwise velocity.

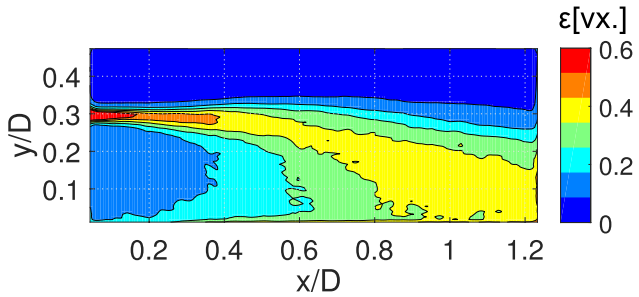

Figure 6. RMS error of streamwise velocity.

flow structures. For flow regions with uniform flow such as the freestream, $\rho_{2\Delta T} \approx 0$ and $c_{|\nabla u|} \approx 0$.

Comparison of both CD results shows that position error propagation and error correlation have a substantial impact on the noise amplification. The error correlation results in a lower error amplification for relatively short tracks (compare solid blue with dashed red line). With increasing track lengths, the impact of correlation decreases, since for longer tracks the velocity errors at the track extremes have a lower correlation (see section 4.2). Meanwhile, for longer tracks the impact of the position error propagation increases (compare figure 2).

3.3. Least-square fitting versus central differencing

So far we have only discussed central differencing and not the least-square fitting (LS) approach. Whereas the errors from LS are discussed extensively in various text books and papers, e.g. Richter (1995)), it is not straightforward to obtain an analytic error expression for LS in case the velocity errors along the track are correlated and do not have a constant variance (i.e. are heteroscedastic), as is the case for pseudo-tracking as discussed above.

For the sake of comparison with CD, we here assume that the track velocity errors have a constant variance (σ_u^2) and are uncorrelated ($\rho_{2\Delta T} = 0$). Under these assumptions, the error variance for LS is

$$\varepsilon^2_{Du/Dt,LS} = \frac{1}{2n_{\mathrm{piv}}}\frac{\sigma_u^2}{\sigma_t^2} = \frac{\sigma_u^2}{2\Delta T^2}\frac{3n_{\mathrm{piv}}}{(n_{\mathrm{piv}}+1)(2n_{\mathrm{piv}}+1)} = \varepsilon^2_{n,LS}\frac{\sigma_u^2}{\Delta t^2_{\mathrm{piv}}}. \quad (5)$$

Here σ_t^2 is the variance of the time scale. Choosing the origin of the time scale symmetrically, this can be expressed as $\sigma_t^2 = (2n)^{-1}\sum_{-n}^{n}(i\Delta t)^2 = \frac{1}{6}\Delta t^2(n+1)(2n+1)$. Note that equation (5) does not include truncation errors. Since CD and LS both assume a linear development of track velocity, it is assumed that they have similar truncation errors (see also part II of this study, van Gent *et al* (2017b)). LS is however expected to be less sensitive to increasing track lengths as it uses velocity data along the full track instead of at the track ends only, as is the case for CD. Comparison to CD (compare blue to yellow line in figure 3 shows that LS is more efficient in reducing the impact of velocity error when adhering to the assumptions made above.

3.4. Errors from interpolation and integration procedures

To investigate the errors introduced by numerical interpolation and integration procedures, we consider that the local truncation error of the integration procedure (ε_{tr}) of order p is bound by $\varepsilon_{tr} \leqslant c_{tr}\Delta t_{\mathrm{int}}^{p+1}$, where c_{tr} is a constant (Süli and Mayers 2013). Furthermore, we consider that the interpolation errors from spatial and temporal linear interpolation are bound by $\varepsilon_{\mathrm{int.spat}} \leqslant \frac{1}{8}h^2\frac{\partial^2 u}{\partial x^2}|_{\max}$ and $\varepsilon_{\mathrm{int.temp}} \leqslant \frac{1}{8}\Delta t^2_{\mathrm{piv}}\frac{\partial^2 u}{\partial t^2}|_{\max}$, respectively, where h is the grid spacing (Süli and Mayers 2013). Assuming a typical PIV measurement in which the seeding particles travel a quarter of the interrogation window size in the freestream and the interrogation window overlap is 75%, this can be combined to $\varepsilon_{\mathrm{int}} \leqslant \frac{1}{8}\Delta t^2_{\mathrm{piv}}\left(\frac{\partial^2 u}{\partial t^2} + U_\infty^2\frac{\partial^2 u}{\partial x^2}\right)_{\max} = c_{\mathrm{int}}\Delta t^2_{\mathrm{piv}}$, where c_{int} is

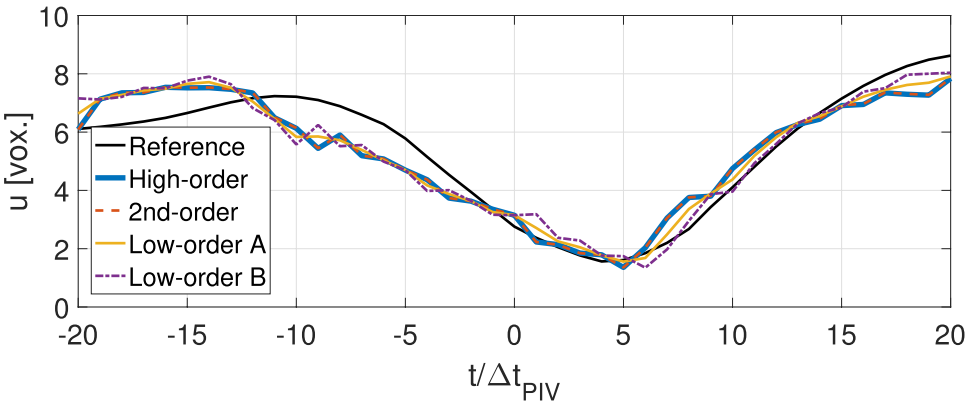

Figure 7. Example track constructions with different numerical procedures.

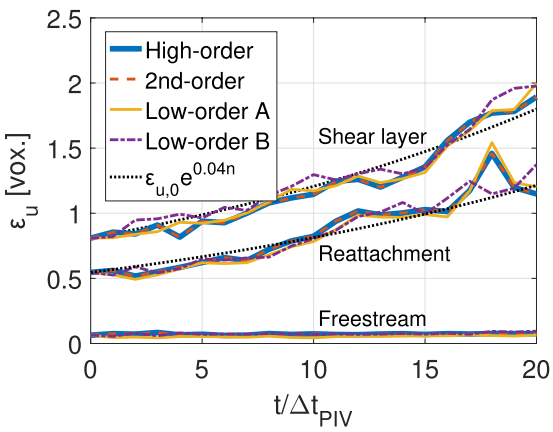

Figure 8. RMS error in streamwise velocity for different numerical procedures (see figure 5 for starting points of tracks).

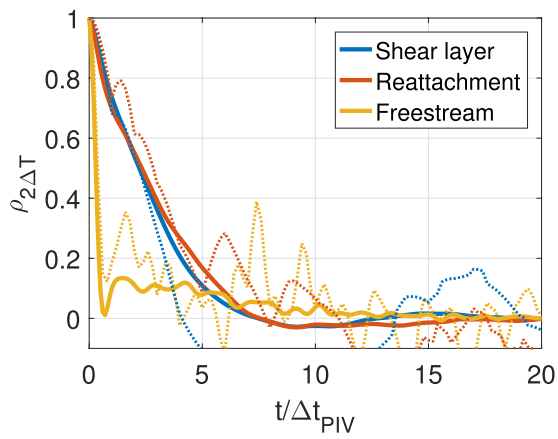

Figure 9. Normalised autocorrelation coefficient of track velocity error for full tracks (solid-lines) and for track ends (dotted lines) (see figure 5 for starting points of tracks).

again a constant. Combining these bounds with the error propagation model discussed in section 3.2 gives (see appendix for derivation):

$$E_{u,n} \leqslant (\varepsilon_{\mathrm{piv,max}} + c_{\mathrm{int}}\Delta t_{\mathrm{piv}}^2 + c_{tr}\Delta t_{\mathrm{int}}^p)\mathrm{e}^{\Delta t L}. \quad (6)$$

Equation (6) shows that if c_{tr} is comparable to c_{int} and Δt_{piv} is comparable to Δt_{int}, a second-order integration scheme is sufficiently accurate with respect to the error from linear interpolation. This is consistent with the results of Teitzel *et al* (1997). Note that in case of pseudo-tracking between only two velocity fields separated by $\Delta T_{\mathrm{piv}} > \Delta t_{\mathrm{piv}}$, the interpolation error bound becomes $\varepsilon_{\mathrm{int}} \leqslant \frac{1}{8}\Delta T_{\mathrm{piv}}^2 \left(\frac{\partial^2 u}{\partial t^2} + \frac{U_\infty^2}{n_{\mathrm{piv}}}\frac{\partial^2 u}{\partial x^2}\right)_{\max}$ instead.

Equation (6) also shows that truncation errors from integration decrease for smaller times steps. Apart from the truncation error, an important consideration when specifying the integration time step is numerical stability. One requirement for stability for explicit numerical integration methods is that the Courant number (C) is smaller than unity so that the Courant–Friedrichs–Lewy (CFL) is met:

$$C = \Delta t_{\mathrm{int}}\left(\frac{u+v+w}{h}\right) \leqslant 1, \quad \Delta t_{\mathrm{int}} \leqslant \frac{h}{u+v+w}. \quad (7)$$

The CFL condition is automatically satisfied in case the PIV experiment is designed so that the particle displacement is smaller than a quarter of the interrogation window size and the interrogation window overlap is 75%. For larger particle displacements or smaller window overlaps, multiple integration/interpolation steps are required between subsequent PIV velocity fields such that $\Delta t_{\mathrm{int}} < \Delta t_{\mathrm{piv}}$.

4. Numerical error assessment

4.1. Description of the test case

A numerical assessment has been performed to test the developed error-analysis framework and further assess the performance of pseudo-tracking. The numerical assessment uses a simulation of the flow over an axisymmetric backward facing step at a freesteam Mach number of 0.7 for which the numerical data were available from van Gent *et al* (2017a), see figure 4. The Reynolds number of the flow is 1.3×10^6 based on the main body diameter. Its richness in terms of spatial and temporal flow scales makes the flow particularly suited to provide a realistic test case for pseudo-tracking.

The PIV experiment was simulated by creating synthetic particle images of a virtual measurement volume located in the domain of a zonal detached eddy simulation (ZDES) (e.g. Weiss *et al* (2009)). Noise was added to the synthetic particle images and all processing steps associated with tomographic PIV were subsequently applied such as to generate

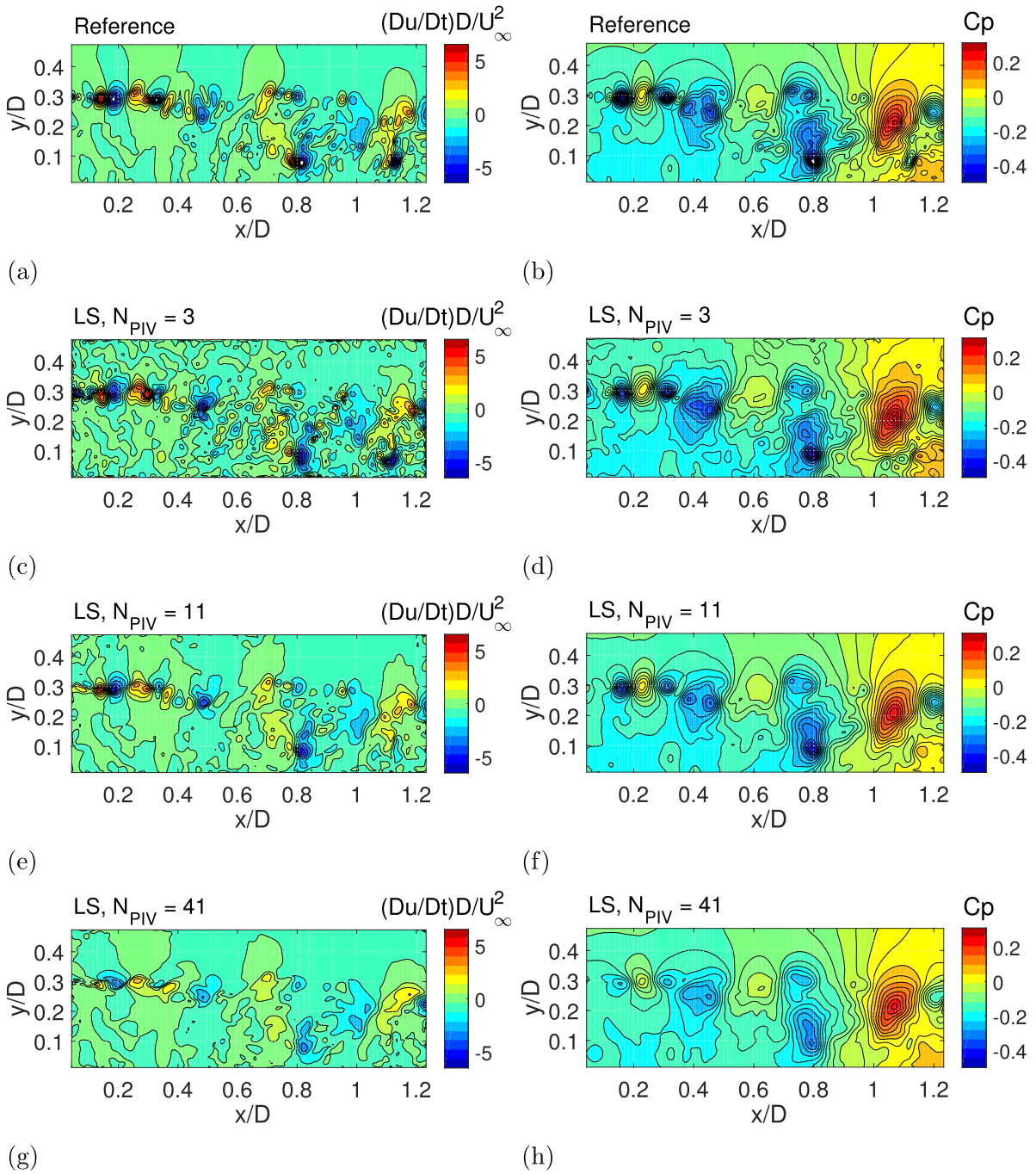

Figure 10. Representative realisation of instantaneous material acceleration in streamwise direction (left) and pressure (right) in the centre-plane for reference data ((a) and (b)) and LS implemented with short ((c) and (d)), optimal ((e) and (f)) and long ((g) and (h)) track lengths.

a data set representative of realistic albeit optimum PIV imaging conditions. The PIV data consist of 4997 velocity fields with a time separation of 2 μs. Each velocity fields contains $171 \times 67 \times 11$ velocity vectors in x-, y- and z-direction, respectively. The reader is referred to van Gent *et al* (2017a) for more information on the numerical simulation and simulated PIV experiment.

Figure 5 depicts a representative example of an instantaneous streamwise velocity field. The figure shows a shear layer that emanates from the corner of the step at $y/D = 0.3$ and grows in downstream direction towards reattachment. The shear layer forms the separation between the fast outer flow and the recirculating inner flow region. The figure indicates three points that will be used in a further analysis: point 1 in the freestream, point 2 in the shear layer, and point 3 in the reattachment region.

Figure 6 shows the RMS error of streamwise velocity, as evaluated by comparing the PIV velocity data to the simulation data interpolated to the PIV grid points. The largest errors are observed in the regions in which the velocity gradients are too large to be properly captured by PIV, i.e. the early shear layer and the highly three-dimensional reattachment region.

4.2. Construction of the imaginary tracks

The three points indicated in figure 5 are used as initial positions for the calculation of imaginary particle paths. Figure 7 shows an example of a track starting in the reattachment region (point 3 in figure 5). Reference tracks have been obtained directly from the ZDES simulation data using 4th-order classical Runge–Kutta integration in combination with natural neighbour interpolation, using five integration steps between each ZDES velocity field. Other tracks are calculated from the PIV velocity fields by different numerical methods:

- High-order: 4th-order classical Runge–Kutta integration in combination with cubic spline interpolation. Five integration steps are performed per PIV time step.
- 2nd-order: Heuns integration scheme in combination with trilinear interpolation. Two integration steps are performed per PIV time step so that the CFL condition is met throughout the full domain.
- Low-order A: Forward Euler in combination with trilinear interpolation. Two integration steps are performed per PIV time step so that the CFL condition is met throughout the domain.
- Low-order B: Same as low-order A, but with one integration step per PIV time step so that the CFL condition is not met throughout the domain.

Figure 7 shows that all tracks calculated from the PIV velocity deviate significantly from the reference track. The results for the different numerical methods are very similar, implying that the respective errors are dominated by the velocity error introduced by the PIV processing. An important observation is that the deviations from the reference track at different time instances are not random in nature.

The track velocity error is calculated as the difference between reference tracks and PIV-based tracks. To investigate the track velocity errors in a statistical sense, figure 8 shows the RMS of the velocity error errors along the tracks starting from the three points indicated in figure 5. Comparison of the different methods in figure 8 shows that the 2nd-order and low-order methods practically yield identical results as the higher-order method if the CFL condition is met. Not meeting the CFL condition leads to slightly higher errors (compare low-order A (CFL condition is met) and low-order B (CFL condition is not met)). The figures show that in the shear layer and reattachment region, the track velocity errors grow away from the initial position in good agreement with the model derived in section 3.2 for $c_{|\nabla u|} \approx 0.04$. No increase in errors is observed in the freestream, where error levels are low.

Figure 9 depicts the average normalised autocorrelation coefficient of the track velocity errors. Solid lines have been obtained by correlating the velocity error along the full track and dotted lines have been obtained by correlating the errors of the particle positions at the track ends separated in time by $2n_{\mathrm{piv}}\Delta t_{\mathrm{piv}}$. The figure shows that the errors in the freestream are largely uncorrelated. In the shear layer and reattachment region where the errors are larger and flow scales are smaller, the correlation is appreciable up to $n_{\mathrm{piv}} = 3{-}5$.

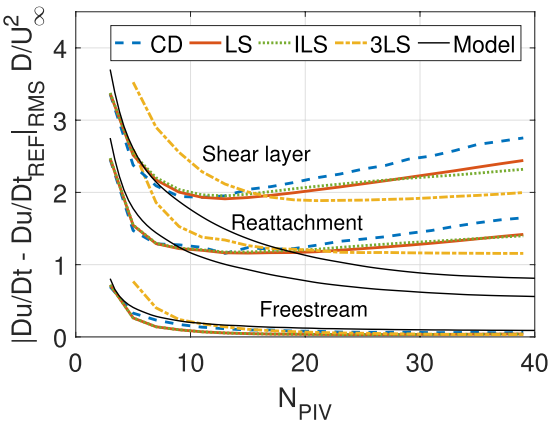

Figure 11. RMS error in acceleration for different approaches and track lengths for the points indicated in figure 5.

4.3. Material acceleration and pressure

Four approaches to calculate the material acceleration from the imaginary particle path are compared: centred differencing (CD), least-square fitting of first-order (LS) and third-order (3LS) polynomials, as well as iterative least-square fitting (ILS) (see section 2). ILS is implemented using 5 iterations after which the result was found to be converged. After calculation of material acceleration fields, pressure fields have been calculated by solving the momentum equation for pressure:

$$\nabla p = -\rho \frac{D\mathbf{u}}{Dt} + \mu \nabla^2 \mathbf{u}. \tag{8}$$

Here ∇p is the local pressure gradient, ρ is the density and μ is the dynamic viscosity. Motivated by the high Reynolds number of the flow, the viscous term (right) is neglected in the pressure reconstruction. Using the simulation data, the contribution of the viscous term to the reconstructed pressure fields was, indeed, found to be at least two orders of magnitude smaller than that of the acceleration term. Equation (8) is discretised according to a three-dimensional implementation of the approach outlined in Jeon *et al* (2015). The resulting (overdetermined) system of linear equations is solved in a least-square sense via the use of QR decomposition. The procedure allows computations on an arbitrarily shaped domain and was checked to perform similarly to pressure reconstruction through a Poisson equation (e.g. Gurka *et al* (1999)) in terms of achieved error levels. Pressure gradients are used implicitly as Neumann boundary conditions on all sides of the domain except for the top. There, the reference pressure values from the simulation data are prescribed as Dirichlet boundary conditions. The pressure is calculated for the full domain and not for the centre-plane only, after a preliminary analysis showed that the pressure errors in the centre plane are lowest if the integration considers all available z-planes (in contrast to Ghaemi *et al* (2012)). The pressure is normalised by first subtracting the freestream static pressure and then dividing the result by the freestream dynamic pressure: $C_p = (p - p_\infty)/(\frac{1}{2}\gamma p_\infty M_\infty^2)$.

Figure 10 shows an instantaneous sample of the material acceleration field in streamwise direction (left figures) calculated with different track lengths as well as the

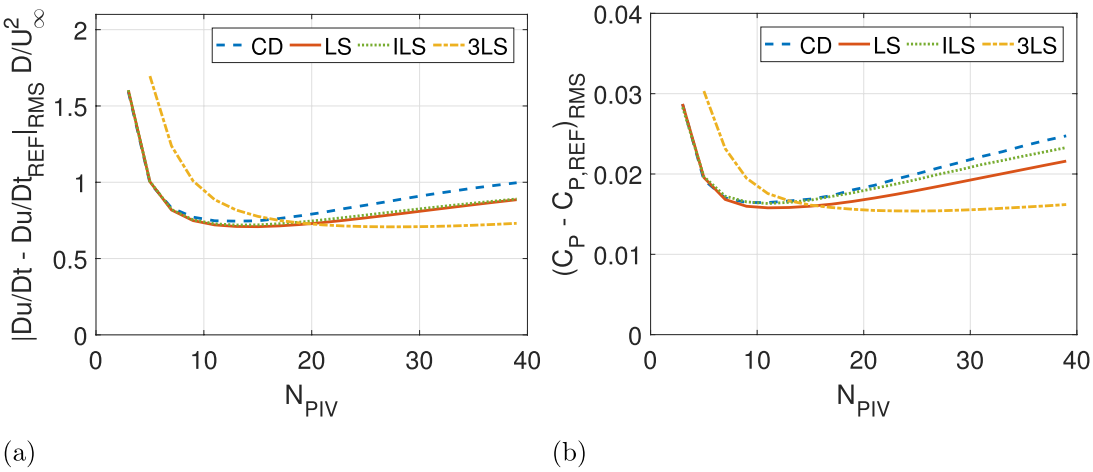

Figure 12. RMS error in (a) acceleration and (b) pressure for different approaches and track lengths, considering all points in the centre plane.

corresponding pressure fields (right figures). Remember that $N_{\text{piv}} = 2n_{\text{piv}} + 1$ is the total number of velocity fields covered by the track. Results have been obtained by LS, but the observations made below also hold of the other approaches. Top figures show the reference data for comparison. All figures correspond to the same time instance.

In general, the material acceleration field shows small-scale, coherent flow structures originating from the corner of the step that break down and interact towards the reattachment region, which is characterised by the presence of flow structures with various length scales. Figures 10(c) and (d) show that the use of short tracks ($N_{\text{piv}} = 3$) leads to noisy material acceleration and pressure fields. The result for an optimal track length that leads to the lowest overall error ($N_{\text{piv}} = 11$), depicted in figures 10(e) and (f), can be characterised as a modulated representation of the reference data. The result shows many of the structures present in the reference data. Small-scale structures, especially near the step and in the reattachment region, are however not reproduced, due to the inherent spatial-temporal filtering of the approach (see part II of this study, van Gent *et al* (2017b)). Results calculated with long tracks ($N_{\text{piv}} = 41$), depicted in figures 10(g) and (h), show that the use of long tracks leads to excessive smoothing.

Figure 11 shows the RMS error in acceleration for the three individual points identified in figure 5, calculated based on 100 snapshots separated from each other by $50\Delta t_{\text{piv}}$. The error is calculated as the difference with the reference data obtained from the numerical simulation data and represents the Euclidean norm of the errors in x-, y, and z-directions. In addition, the figure includes the velocity error propagation calculated according to equation (4) using position error propagation constants ($c_{|\nabla u|}$) and error correlation functions ($\rho_{2\Delta T}$) as shown in figures 8 and 9.

Figure 12 shows the global RMS acceleration and pressure errors based on all points in the centre plane, as a function of the nominal track length. Because tracks are cut-off at the boundaries of the domain, the average effective track length is smaller than the nominal track length, e.g. for a nominal track length of $N_{\text{nom}} = 27$, the average effective track length is $\overline{N_{\text{eff}}} = 23$. Calculating tracks over more and more snapshots becomes less and less effective as an increasing amount of imaginary particles leaves the measurement domain. Note that the pressure error (figure 12(b)) not only depends on the acceleration error (figure 12(a)), but also on the subsequent spatial integration, hence, on the (type of) boundary conditions and the dimensions of the domain (Pan *et al* 2016).

The figures shows that as the track length increases, all methods initially exhibit a strong reduction of the total error which is attributed to reduced impact of the velocity measurement errors. The initial error level and its reduction compare favourably to the model expressed by equation (4) indicating its validity. After attaining a minimum, the errors increase, which is attributed to increasing truncation errors and path reconstruction errors.

Comparison of the results obtained with different methods shows that all methods achieve a similar minimum error level, but differ in terms of their working range, i.e. the range of track lengths for which the error remains close to its minimum value. CD has a relatively short working range which is attributed to the fact that CD only uses the track extremes instead of the full track as the other methods do. 3LS requires a relatively long track to reach its minimum error level, but has the longest working range. ILS performs very similar to LS showing no benefit from adopting an iterative approach. This does however not mean that iterative approaches have no benefits when applied to other (test) cases, e.g. with higher velocity noise levels.

Figure 11 shows that the optimal track length varies throughout the measurement domain. In the shear layer, where flow scales are predominantly small, the optimal track length is relatively short. In the freestream, where flow is relatively steady with limited curvature the optimal track length is relatively long. It is therefore tempting to think of adaptive approaches that locally use a different track lengths or that locally adjust the order of the fitted polynomial (see, e.g. Wang *et al* (2017)). Several variations to such approaches have been considered as part of this study. None of the approaches tested did however result in lower overall RMS errors. Speculatively, this is because the global error is dominated by regions with

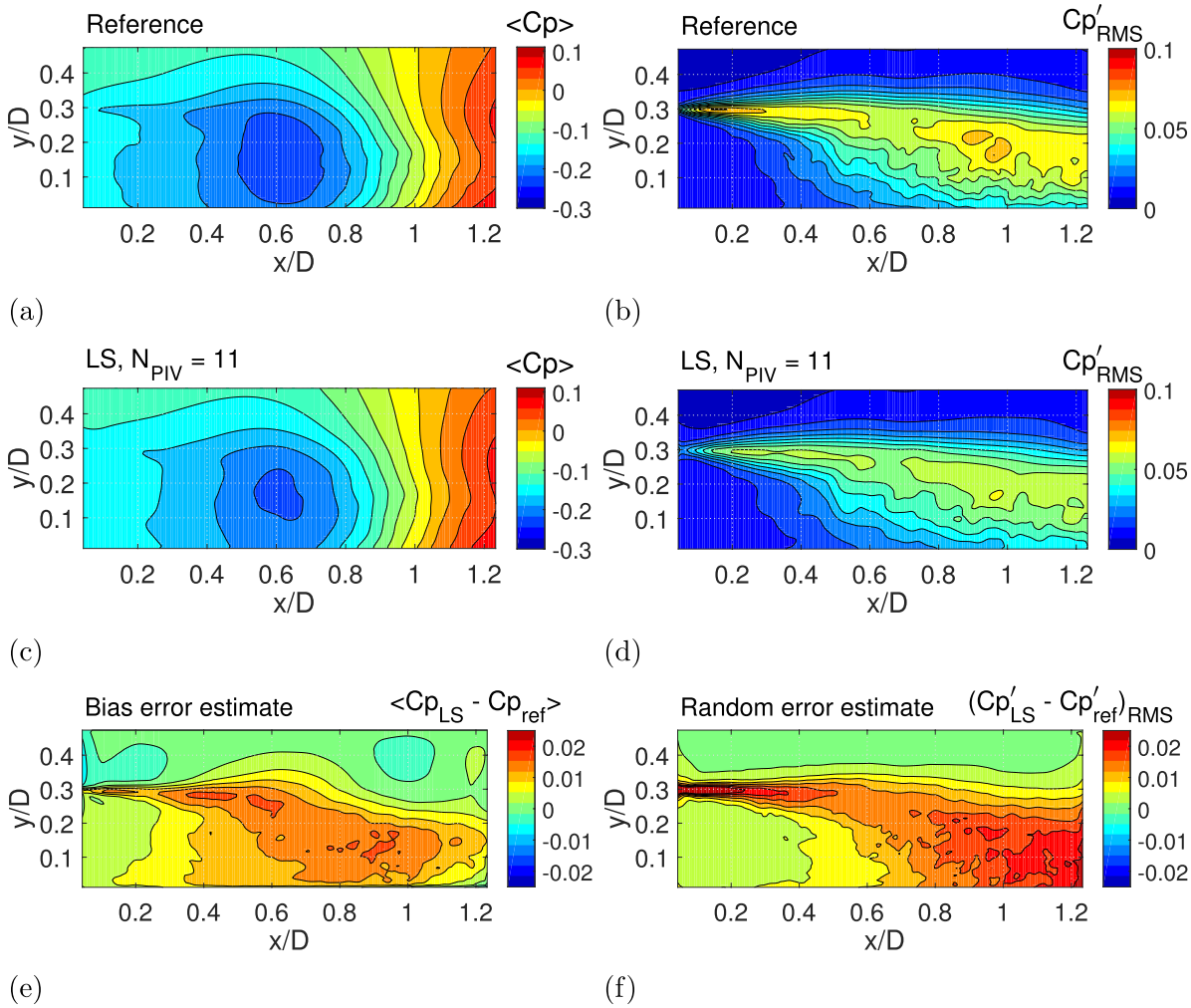

Figure 13. Ensemble-average pressure and RMS of pressure fluctuations from reference data ((a) and (b)) and as reconstructed via LS approach ((c) and (d)); bias error estimate (e) and random error estimate (f). All figures show the centre plane.

small scales, as the errors in the regions without small flow scales such as the freestream are low anyway. Also, closer inspection of figure 11 shows that the working range of different approaches for the different locations partially overlap, so that it is possible to obtain relatively low errors with a globally prescribed track length.

Figure 13 compares the calculated pressure fields to the reference pressure, for the centre plane of the domain. The top row shows the reference mean pressure and pressure fluctuation levels. The centre row shows the results obtained with LS with an optimal track length of $N_{\mathrm{piv}} = 11$. The bottom row compares the reconstructed pressure solution to the reference by showing the mean difference as a measure for the bias error and the standard deviation of the difference as a measure for the random error. All statistical quantities are based on instantaneous pressure fields for 4900 time instances.

The mean reference and mean reconstructed pressure fields show similar features, with the mean values of reconstructed pressure fields being slightly higher (compare figures 13(a) and (c)). Note this is not due to errors in the Dirichlet boundary condition, which was set to be equal to the reference pressure. Pressure fluctuation levels for the reconstructed pressure fields are lower than the reference fluctuation levels (compare figures 13(b) and (d)). The random error estimate has a similar order of magnitude as the mean error estimate (compare figures 13(e) and (f)) and has a substantial magnitude compared to the reconstructed fluctuation levels (figure 13(d)).

To further compare the reference and reconstructed pressure fields, figure 14 shows the normalised correlation coefficient in the centre plane. The figures shows typical values ranging from close to 1 in the freestream to around 0.85 near the bottom of the domain.

5. Estimation of optimal track length

To assess what range of (pseudo-)track lengths results in relatively low total error levels, it is considered that any random errors in the material acceleration contribute to the observed fluctuation levels (of the material acceleration). The variation in fluctuation levels with track length may therefore be used as an indicator for the development of the overall error. To further investigate this idea, figure 15 shows the RMS of the Euclidean norms of all material acceleration vectors in the field of view as a function of track length. The RMS is based on all points in the field of view for a single snapshot.

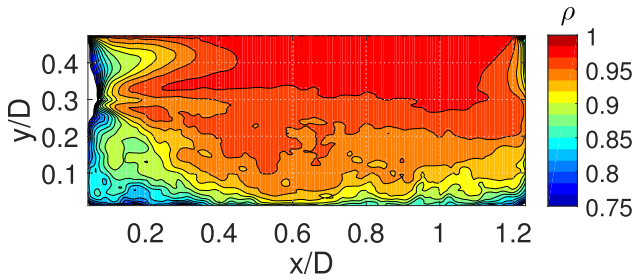

Figure 14. Normalised correlation between reference and reconstructed pressure (LS, $N_{\mathrm{piv}} = 11$).

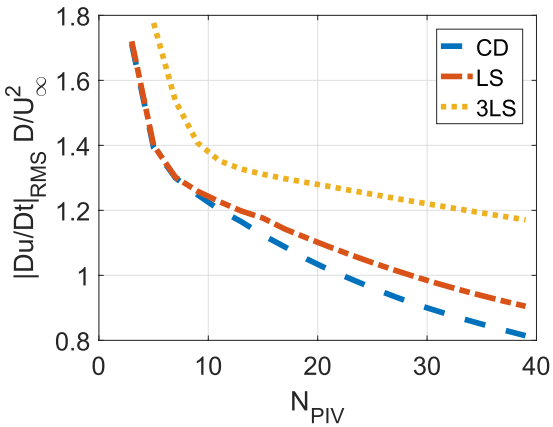

Figure 15. RMS of the norms of all material acceleration vectors in a single snapshot as a function of track length, for different methods.

The figure shows a similar development for the different methods: a relatively strong drop is followed by a more gradual change. The initial drop is attributed to a reduction in random errors. The more gradual decrease is attributed to modulation (smoothening) of the material acceleration field and is associated with increasing truncation errors. Comparison with figure 11 indeed shows that the relatively strong drop over the range $N_{\mathrm{piv}} = 3{-}7$ for CD and LS is accompanied by a strong decrease in overall error. Similarly, the more gradual change for $N_{\mathrm{piv}} > 11$ is accompanied by a gradual increase of error levels. The minimum overall error is attained shortly after the transition of both regimes. Similarly for 3LS, the relatively steep drop occurs over $N_{\mathrm{piv}} < 15$ which again corresponds to the range over which the overall error decreases (compare figure 11).

These observations put in evidence that the RMS of the norms of all material acceleration vectors in a single snapshot can indeed be used as an indicator for the development of errors with track length. Although a robust quantitative criterion to select an optimal track length could not be defined, it is suggested as guideline for experimental investigations to select a track length shortly after the initial, relatively steep drop of the value of this indicator.

6. Conclusions

The current study presents a theoretical and numerical error assessment of the pseudo-tracking method for the determination of material acceleration fields, and subsequently pressure fields, from time-resolved PIV measurements. The findings of the investigation allow to formulate the following insights and guidelines for its use:

(i) The velocity errors along the imaginary particle track are only weakly dependent on the numerical procedures used and are primarily a function of the direct velocity measurement error and spatial velocity gradients. As a result of error propagation, the track velocity error may increase exponentially with track length. When modelling the velocity error propagation in flow regions with spatial velocity gradients and unresolved flow scales, it is essential to consider the correlation of velocity errors along the track.

(ii) For the calculation of the imaginary particle track, a second-order integration scheme in combination with linear interpolation provides sufficient accuracy with respect to the velocity errors. The integration time step should be chosen such that the Courant number is smaller than unity and the CFL condition is met.

(iii) Least-square fitting of a first-order polynomial (LS) is a suitable method to estimate the derivative of the track velocity. The method achieves similarly low error levels as centred differencing (CD) but exhibits a longer range of track lengths for which the error is relatively low (working range). Least-square fitting of third-order polynomials (3LS) has a longer working range than the first-order approach (LS), but requires longer tracks to achieve similarly low error levels.

(iv) No reduction in the global error levels could be achieved by using locally adaptive track lengths, by locally adjusting the order used during least-square polynomial fitting, or by using the result of a least-square fit to recalculate the track in a next iteration (iterative least-square fitting, ILS). This does however not mean that such approaches in general have no benefits when applied to other flow cases and to velocity fields with different resolutions and/or noise levels.

(v) The variation in the RMS of the norms of all material acceleration vectors in a single snapshot may be used as an indicator for the development of errors with track length. It is suggested as guideline for experimental investigations to select a track length shortly after an initial, relatively steep drop of the value of this indicator.

Following the present investigation of error propagation in the pseudo-tracking method, part 2 of this study characterises its spatio-temporal filtering behaviour (van Gent *et al* 2017b).

Finally, it is noted that it remains an open question whether noise reduction can best be achieved by filtering the input velocity data, elongating the track length, including filtering as part of an iterative procedure, or filtering the acceleration or pressure output.

Acknowledgments

This work is supported by the European FP7 project NIOPLEX, grant agreement 605151.

Appendix

The local position error (ε_x) is the error that is incurred during a single integration step. When performing multiple integration steps, the local position error from previous steps leads to a velocity error in the presence of a velocity gradients. The global (total) position error $E_{x,i}$ integration steps with time step Δt is

$$\mathbf{E_{x,i+1}} = \varepsilon_{\mathbf{x,i}} + (\mathbf{I} + \Delta t \mathbf{J}(\mathbf{u}))\mathbf{E_{x,i}} \leqslant \varepsilon_{x,\max} + (1 + \Delta t L)E_i \quad \mathbf{E_{x,0}} = \mathbf{0}. \quad (A.1)$$

Here, $\varepsilon_{x,i}$ is the local position error incurred at integration step i, and $(\mathbf{I} + \Delta t \mathbf{J}(\mathbf{u}))\mathbf{E_{x,i}}$ represents the propagation of the position errors from previous steps. $\mathbf{I}$ is the identity matrix, $\mathbf{J}(\mathbf{u})$ is the Jacobian of $\mathbf{u}$, $\varepsilon_{x,\max}$ is the maximum local error in any direction and L is the Lipschitz constant according to

$$||\mathbf{u}(\mathbf{x_1}, t_1) - \mathbf{u}(\mathbf{x_2}, t_2)||L \leqslant ||\mathbf{x_1} - \mathbf{x_2}||. \quad (A.2)$$

For all x_1, x_2 and t_1 and t_2 in the domain of u. Equation (A.1) can be used to define a geometric series that bounds the global error after n_{int} integration steps (Süli and Mayers 2013). For brevity, the derivation uses $n = n_{\text{int}}$. Using $Q = (1 + \Delta t L)$:

$$E_{x,i} \leqslant \varepsilon_{x,\max} \sum_{i=0}^{n-1} Q^i = \varepsilon_{x,\max} \frac{1 - Q^n}{1 - Q} = \varepsilon_{x,\max} \frac{Q^n - 1}{\Delta t L} \leqslant \varepsilon_{x,\max} \frac{e^{L\Delta T} - 1}{\Delta t L} \quad (A.3)$$

where $2\Delta T = 2n\Delta t$ is the total time covered by the track. The local position error ($\varepsilon_{\mathbf{x}}$) is composed of the local truncation error from integration ($\varepsilon_{\mathbf{tr}}$) and the propagation of velocity errors ($\varepsilon_{\mathbf{u}}$), and is bound by

$$\varepsilon_{x,\max} \leqslant \varepsilon_{\text{x,max}} + \varepsilon_{u,\max}\Delta t. \quad (A.4)$$

The global velocity error can be expressed as

$$\mathbf{E_{u,n}} = \varepsilon_{\mathbf{u}} + \mathbf{J}(\mathbf{u})\mathbf{E_{x,n}} \quad (A.5)$$

where $\mathbf{J}(\mathbf{u})\mathbf{E_{x,n}}$ represents the impact of position errors in the presence of velocity gradients. Inserting equations (A.3) and (A.4), a bound for the global velocity error is obtained:

$$E_{u,n} \leqslant \varepsilon_{u,\max} + E_{x,n}L \leqslant \varepsilon_{u,\max} + \varepsilon_{x,\max} \frac{e^{L\Delta T} - 1}{\Delta t} \leqslant \varepsilon_{u,\max} e^{L\Delta T} + \varepsilon_{\text{x,max}} \frac{e^{L\Delta T} - 1}{\Delta t} \leqslant (\varepsilon_{u,\max} + \varepsilon_{\text{x,max}}\Delta t^{-1})e^{L\Delta T}. \quad (A.6)$$

The local velocity error (ε_u) incorporates both the measurement error (ε_{piv}) and the residual errors from spatial and temporal interpolation (ε_{int}). The interpolation errors are zero at the sampling locations and for linear interpolation reach a maximum at an intermediate location, bound to $\varepsilon_{\text{int.spat}} \leqslant \frac{1}{8}h^2 \frac{\partial^2 u}{\partial x^2}|_{\max}$ and $\varepsilon_{\text{int.temp}} \leqslant \frac{1}{8}\Delta t_{\text{piv}}^2 \frac{\partial^2 u}{\partial t^2}|_{\max}$, respectively (Süli and Mayers 2013). Assuming a typical PIV measurement in which the seeding particles travel a quarter of the interrogation window size in the freestream and the interrogation window overlap is 75%, this can be combined to

$$\varepsilon_{\text{int}} \leqslant \frac{1}{8}\Delta t_{\text{piv}}^2 \left(\frac{\partial^2 u}{\partial t^2} + U_\infty^2 \frac{\partial^2 u}{\partial x^2} \right)_{\max} = c_{\text{int}}\Delta t_{\text{piv}}^2 \quad (A.7)$$

where c_{int} is a constant. The local truncation error of the integration procedure (ε_{tr}) of order p is bounded by $\varepsilon_{tr} \leqslant c_{tr}\Delta t^{p+1}$, where c_{tr} is a constant (Süli and Mayers 2013). Combining these bounds with equation (A.6), gives

$$E_{u,n} \leqslant (\varepsilon_{\text{piv,max}} + c_{\text{int}}\Delta t_{\text{piv}}^2 + c_{tr}\Delta t_{\text{int}}^p)e^{L\Delta T}. \quad (A.8)$$

ORCID iDs

P L van Gent https://orcid.org/0000-0001-9972-1681

References

Ahnert K and Abel M 2007 Numerical differentiation of experimental data: local versus global methods *Comput. Phys. Commun.* **177** 764–74

Baur T and Köngeter J 2002 PIV with high temporal resolution for the determination of local pressure reductions from coherent turbulence phenomena *3rd Int. Workshop on Particle Image Velocimetry* (*Santa Barbara, CA*)

Christensen K and Adrian R 2002 Measurement of instantaneous Eulerian acceleration fields by particle image accelerometry: method and accuracy *Exp. Fluids* **33** 759–69

Dabiri J O, Bose S, Gemmell B J, Colin S P and Costello J H 2014 An algorithm to estimate unsteady and quasi-steady pressure fields from velocity field measurements *J. Exp. Biol.* **217** 331–6

de Kat R and van Oudheusden B W 2012 Instantaneous planar pressure determination from PIV in turbulent flow *Exp. Fluids* **52** 1089–106

Foucaut J M and Stanislas M 2002 Some considerations on the accuracy and frequency response of some derivative filters applied to particle image velocimetry vector fields *Meas. Sci. Technol.* **13** 1058–71

Gesemann S, Huhn F, Schanz D and Schröder A 2016 From particle tracks to velocity and acceleration fields using B-splines and penalties *18th Int. Symp. on the Application of Laser, Imaging Techniques to Fluid Mechanics (Lisbon, Portugal)*

Ghaemi S, Ragni D and Scarano F 2012 PIV-based pressure fluctuations in the turbulent boundary layer *Exp. Fluids* **53** 1823–40

Ghaemi S and Scarano F 2013 Turbulent structure of high-amplitude pressure peaks within the turbulent boundary layer *J. Fluid Mech.* **735** 381–426

Gorry P 1990 General least-squares smoothing and differentiation by the convolution method *Anal. Chem.* **62** 570–3

Gurka R, Liberzon A, Rubinstein D and Shavit U 1999 Computation of pressure distribution using PIV velocity data *3rd Int. Workshop on Particle Image Velocimetry (Santa Barbara, CA)*

Jeon Y J, Chatellier L and David L 2014 Fluid trajectory evaluation based on an ensemble-averaged cross-correlation in time-resolved PIV *Exp. Fluids* **55** 1766

Jeon Y J, Chatellier L, Beaudoin A and David L 2015 Least-square reconstruction of instantaneous pressure field around a body based on a directly acquired material acceleration in time-resolved PIV *11th Int. Symp. on Particle Image Velocimetry (Santa Barbara, CA)*

Jeon Y J, Earl T, Braud P, Chatellier L and David L 2016 3D pressure field around an inclined airfoil by tomographic TR-PIV and its comparison with direct pressure measurements *18th Int. Symp. on the Application of Laser and Imaging Techniques to Fluid Mechanics (Lisbon, Portugal)*

Jensen A and Pedersen G K 2004 Optimization of acceleration measurements using PIV *Meas. Sci. Technol.* **15** 2275–83

Jensen A, Pedersen G K and Wood D J 2003 An experimental study of wave run-up at a steep beach *J. Fluid Mech.* **486** S0022112003004543

Joshi P, Liu X and Katz J 2014 Effect of mean and fluctuating pressure gradients on boundary layer turbulence *J. Fluid Mech.* **748** 36–84

Knowles I and Renka R J 2012 Methods for numerical differentiation of noisy data *Electron. J. Differ. Equ. Conf.* 21 235–46

Laskari A, de Kat R and Ganapathisubramani B 2016 Full-field pressure from snapshot and time-resolved volumetric PIV *Exp. Fluids* **57** 44

Liu X and Katz J 2006 Instantaneous pressure and material acceleration measurements using a four-exposure PIV system *Exp. Fluids* **41** 227–40

Liu X and Katz J 2013 Vortex-corner interactions in a cavity shear layer elucidated by time-resolved measurements of the pressure field *J. Fluid Mech.* **728** 417–57

Lynch K and Scarano F 2013 A high-order time-accurate interrogation method for time-resolved PIV *Meas. Sci. Technol.* **24** 035305

McClure J and Yarusevych S 2017 Optimization of planar PIV-based pressure estimates in laminar and turbulent wakes *Exp. Fluids* **58** 62

Moore P, Lorenzoni V and Scarano F 2011 Two techniques for PIV-based aeroacoustic prediction and their application to a rod-airfoil experiment *Exp. Fluids* **50** 877–85

Pan Z, Whitehead J, Thomson S and Truscott T 2016 Error propagation dynamics of PIV-based pressure field calculations: how well does the pressure poisson solver perform inherently? *Meas. Sci. Technol.* **27** 84012

Perret L, Braud P, Fourment C, David L and Delville J 2006 3-Component acceleration field measurement by dual-time stereoscopic particle image velocimetry *Exp. Fluids* **40** 813–24

Pröbsting S, Scarano F, Bernardini M and Pirozzoli S 2013 On the estimation of wall pressure coherence using time-resolved tomographic PIV *Exp. Fluids* **54** 1567

Raffel M, Willert C E, Wereley S T and Kompenhans J 2007 *Particle Image Velocimetry* (*Experimental Fluid Mechanics*) 2nd edn (Berlin: Springer)

Richter P H 1995 Estimating errors in least-squares fitting *TDA Progress Report* pp 42–122

Scarano F 2013 Tomographic PIV: principles and practice *Meas. Sci. Technol.* **24** 012001

Schanz D, Gesemann S and Schröder A 2016 Shake-The-Box: Lagrangian particle tracking at high particle image densities *Exp. Fluids* **57** 70

Schneiders J F G and Scarano F 2016 Dense velocity reconstruction from tomographic PTV with material derivatives *Exp. Fluids* **57** 139

Schrijer F F J and Scarano F 2008 Effect of predictor-corrector filtering on the stability and spatial resolution of iterative PIV interrogation *Exp. Fluids* **45** 927–41

Süli E and Mayers D F 2013 *An Introduction to Numerical Analysis* 1st edn (Cambridge: Cambridge University Press)

Teitzel C, Grosso R and Ertl T 1997 Efficient and reliable integration methods for particle tracing in unsteady flows on discrete meshes *Proc. of 8th Eurographics Workshop on Visualization in Scientific Computing* 4 49–56

van Gent P L *et al* 2017a Comparative assessment of pressure field reconstructions from particle image velocimetry measurements and lagrangian particle tracking *Exp. Fluids* **58** 33

van Gent P L, Schrijer F and van Oudheusden B 2017b Assessment of the pseudo-tracking approach for the calculation of material acceleration and pressure fields from time-resolved PIV: part II. Spatio-temporal filtering behaviour *Meas. Sci. Technol.* **29** 045206

van Oudheusden B W 2013 PIV-based pressure measurement *Meas. Sci. Technol.* **24** 032001

Violato D, Moore P and Scarano F 2011 Lagrangian and eulerian pressure field evaluation of rod-airfoil flow from time-resolved tomographic PIV *Exp. Fluids* **50** 1057–70

Wang Z, Gao Q, Pan C, Feng L and Wang J 2017 Imaginary particle tracking accelerometry based on time-resolved velocity fields *Exp. Fluids* **58** 113

Weiss P E, Deck S, Robinet J C and Sagaut P 2009 On the dynamics of axisymmetric turbulent separating/reattaching flows *Phys. Fluids* **21** 075103